

Supercurrent and multiple Andreev reflections in an InSb nanowire Josephson junction

H. A. Nilsson,[†] P. Samuelsson,[‡] P. Caroff,[¶] and H. Q. Xu^{*,†,§}

Division of Solid State Physics, Lund University, P.O. Box 118, S-221 00 Lund, Sweden, Division of Mathematical Physics, Lund University, P.O. Box 118, S-221 00 Lund, Sweden, and I.E.M.N., UMR CNRS 8520, Avenue Poincaré, BP 60069, F-59652 Villeneuve d'Ascq, France

E-mail: Hongqi.Xu@ff.lth.se

Abstract

Epitaxially grown, high quality semiconductor InSb nanowires are emerging material systems for the development of high performance nanoelectronics and quantum information processing and communication devices, and for the studies of new physical phenomena in solid state systems. Here, we report on measurements of a superconductor-normal conductor-superconductor junction device fabricated from an InSb nanowire with aluminum based superconducting contacts. The measurements show a proximity induced supercurrent flowing through the InSb nanowire segment, with a critical current tunable by a gate, in the current bias configuration and multiple Andreev reflection characteristics in the voltage bias configuration. The temperature dependence and the magnetic field dependence of the critical current and the multiple Andreev reflection characteristics of the junction are also studied. Furthermore, we extract

*To whom correspondence should be addressed

[†]Division of Solid State Physics, Lund University, P.O. Box 118, S-221 00 Lund, Sweden

[‡]Division of Mathematical Physics, Lund University, P.O. Box 118, S-221 00 Lund, Sweden

[¶]I.E.M.N., UMR CNRS 8520, Avenue Poincaré, BP 60069, F-59652 Villeneuve d'Ascq, France

[§]Key Laboratory for the Physics and Chemistry of Nanodevices and Department of Electronics, Peking University, Beijing 100871, China

the excess current from the measurements and study its temperature and magnetic field dependences. The successful observation of the superconductivity in the InSb nanowire based Josephson junction device indicates that InSb nanowires provide an excellent material system for creating and observing novel physical phenomena such as Majorana fermions in solid state systems.

Keywords: InSb nanowires, Josephson junction, supercurrent, multiple Andreev reflection

Epitaxially grown semiconductor nanowires are emerging nanomaterials with potential applications in nanoelectronics and optoelectronics.^{1–20} Novel wrap-gate field-effect transistors,^{15–19} light emitting devices,^{3–7} and photovoltaic devices^{8–12} have been proposed and developed with these high crystalline-quality nanowires. These nanowires are also highly desirable nanomaterials for realizing novel physical systems in the parameter space suitable for the investigations of physical phenomena arising from the strong quantum confinement, Coulomb interaction, and spin correlation.^{21–25} Here, the intrinsic one-dimensional geometrical structure of the nanowires has greatly simplified the device fabrication process. In addition, a variety of metal contact combinations can be employed, opening up great possibilities in the realization of hybrid devices^{26–31} for new physics studies. Among them, epitaxially grown, high crystalline-quality InSb nanowires^{22,32,33} are one of most interesting material systems, due to the fact that bulk InSb material^{34,35} has a very high electron mobility $\mu_e \sim 77000 \text{ cm}^2/\text{Vs}$, a very small electron effective mass $m_e^* \sim 0.015 m_e$, and a very large electron magnetic moment $|g^*| \sim 51$. Recently, quantum dot devices manufactured from InSb nanowires have shown to exhibit giant, strongly level-dependent electron g-factors and strong spin-orbit interactions.²² As a result, InSb nanowires have been suggested as one of most promising material systems for creating novel particles—Majorana fermions—in solid state systems.^{36–42} However, one of the prerequisites for creating Majorana fermions in an InSb nanowire based device is to introduce superconductivity in the nanowire device by the proximity effect. Thus, an experimental verification of the proximity induced superconductivity in the InSb nanowires is an important step towards realizing Majorana fermions in solid state structures.

Here, we report a first experimental study of a superconductor-normal conductor-superconductor

(S-N-S) junction device fabricated from the InSb nanowire segment of an InSb/InAs nanowire heterostructure with aluminum based superconducting contacts. The measurements show a proximity induced supercurrent flowing through the InSb nanowire junction, with a critical current tunable by a gate, and multiple Andreev reflection (MAR) characteristics. The temperature dependence and the magnetic field dependence of the critical current and the MAR characteristics of the InSb nanowire based S-N-S junction device are also studied in details. Furthermore, we extract the excess current from the measurements and study its temperature and magnetic field dependences. The successful observation of the proximity induced superconductivity in the S-N-S junction device indicates that InSb nanowires provide an excellent solid state system for creating and observing Majorana fermions.

The InSb nanowire based S-N-S junction devices investigated here are fabricated from InSb segments of InSb/InAs heterostructure nanowires. The heterostructure nanowires are grown on InAs(111)B substrates by metal-organic vapor phase epitaxy in a two-stage approach using aerosol gold particles with a diameter of 40 nm as initial seeds.^{22,32} In the first stage of growth, the InAs nanowire segments are grown from the gold particles using precursor materials of trimethylindium (TMIn) and arsine. In the second stage of growth, arsine is switched to trimethylantimony (TMSb) and the grown InAs segments serve as seeds to favor nucleation of InSb. Moreover, the grown InAs segments have ensured physical decoupling of the top InSb segment growth and substrate surface growth, thus favoring stable and reproducible growth of InSb nanowires. At the heterostructure interfaces, the diameter of the nanowires increases substantially after the precursor switch due to an increase in the indium content in the metal particles. Thus, the grown InSb nanowire segments have a larger diameter than the InAs nanowire segments, as clearly visible in 1a. For further details about the growth and structural properties of the InAs/InSb heterostructure nanowires employed in this work, we refer to Refs. 22 and 32.

The grown InAs/InSb heterostructure nanowires are transferred to a SiO₂ capped, degenerately doped, n-type Si substrate with predefined Ti/Au bonding pads and metal markers. Using an optical microscope, the wire positions relative to the metal markers are recorded. The substrate is then

spin-coated with poly(methyl methacrylate) (PMMA) resist. Using electron beam lithography, two 200-nm-wide contact areas with a varying spacing between them are defined on the InSb segment of each selected heterostructure nanowire. To obtain a clean metal-semiconductor interface, the exposed semiconductor contact areas are briefly etched in a $(\text{NH}_4)_2\text{S}_x$ solution, followed by a rinse in H_2O before metal deposition. Finally, metal contact electrodes are defined by vapor deposition of 5-nm-thick Ti and 85-nm-thick Al metal, and a process of lift-off in hot acetone. A scanning electron microscope (SEM) image of a fabricated device is shown in 1a. The room-temperature resistance of fabricated devices is measured using a probe station and the devices with room-temperature resistance in the order of $10\text{ k}\Omega$ are selected for detailed studies at low temperatures. In this work, we report the results of low-temperature electrical measurements of a selected device as shown in 1a with a spacing of 30 nm between the two superconductor contacts—a device among the shortest nanowire-based S-N-S junctions. All electrical measurements presented below are performed in a $^3\text{He}/^4\text{He}$ dilution refrigerator.

1b shows the V-I characteristics of the device at a cryostat base temperature of 25 mK. Here the source-drain voltage V_{sd} is measured as a function of the applied source-drain current I_{sd} at back gate voltages $V_{bg} = -1.5, -1.1, \text{ and } -1.0\text{ V}$. In this figure, the measured voltages for both current sweep directions are plotted, where the black curves are for the upward current sweeps and the red curves are for the downward current sweeps. The measured V-I characteristics exhibit a clear superconductive branch (i.e., a zero resistance region) and a dissipative quasiparticle branch. The appearance of the dissipationless supercurrent in the device is a clear manifestation of the proximity effect, which can be viewed as a consequence of the diffusion of Cooper pairs through the entire nanowire section between the two superconducting contacts. The switching between the superconductive and the dissipative branch depends on the back gate voltage and the sweeping direction of the source-drain current. At a given back gate voltage, the switching from superconductive to dissipative conduction occurs when the current approaches a critical value I_c , leading to an abrupt appearance of a finite voltage. The reversed switching from resistive to superconductive state may not occur at the same critical value of the current, but a lower current level I_r , as seen in

the measured V-I curve at the back gate voltage $V_{bg} = -1.5$ V. This hysteretic behavior, which has also been seen in Josephson junctions made from InAs nanowires²⁶ and from Si/Ge nanowires,²⁸ could be the result of phase instability typically found in a capacitively and resistively shunted Josephson junction or simply due to a heating effect.^{43,44}

1c displays the differential resistance dV_{sd}/dI_{sd} , on a color scale, as a function of source-drain current I_{sd} and back gate voltage V_{bg} at the base temperature of $T = 25$ mK. Here, only the data recorded in the upward current sweeps are used in deriving the differential resistance dV_{sd}/dI_{sd} and thus the dV_{sd}/dI_{sd} plot is slightly asymmetric with respect to the zero current at some back gate voltages, due to the hysteretic effect discussed above. The dark central area in 1c corresponds to a superconductive region with negligibly low device resistance and the critical current I_c can be identified at the right edge of the dark area. It is clearly seen that the critical current I_c is a function of V_{bg} . This is a unique feature for a Josephson junction with the junction link made from a semiconductor, since the critical current I_c is related to the resistance R_n of the link in the normal state^{43,45} as $I_c R_n \sim \Delta/e$ at temperature well below T_c and the resistance R_n can be tuned by a gate in a semiconductor based junction device. Also, there exist two distinct regions of back gate voltages in which the critical current I_c is large: the region around $V_{bg} = -1$ V and the region with $V_{bg} > 0$ V. In the region around $V_{bg} = -1$ V, the critical current I_c shows a smooth variation and in the other region the critical current I_c shows rapid fluctuations as a function of V_{bg} .

To understand the appearance of the distinct characteristics of the critical current I_c in the two back gate voltage regions, we measure the normal state conductance G_n of the InSb nanowire junction device and plot the results (red solid curve) along with the measured critical current I_c (black dots) in 2a. The measurements of the normal state conductance G_n are made at $T = 25$ mK by applying a magnetic field $B = 100$ mT, sufficiently larger than the critical magnetic field of the Al electrodes, to the device in the linear response regime. It is seen in 2a that the normal state conductance G_n of the InSb nanowire junction shows a broad resonant peak on a conductance background of about $2e^2/h$ with the peak value close to $4e^2/h$ at $V_{bg} \sim -1$ V and rapid fluctuations around $4e^2/h$ at $V_{bg} > 0$ V. The resonant peak can be attributed to transport through a broadened energy

level in the InSb nanowire junction, while the rapid fluctuations resemble mesoscopic conductance fluctuations of a coherent, quasi-ballistic or diffusive conductor, indicating that the transport in the InSb nanowire section is quasi-ballistic or diffusive at $V_{bg} > 0$ V. In addition, the overall measured normal state conductance values are in the range of $2e^2/h$ to $4e^2/h$ at the back gate voltages of -3 V to 2 V, implying that the normal state transport in the InSb nanowire section is in the few-channel regime in this back gate voltage range. 2a also clearly shows that the Josephson critical current I_c of the device is correlated closely to the normal state conductance G_n of the InSb nanowire junction. Furthermore, it is seen that the relative amplitudes of the critical current fluctuations $\delta I_c/I_c$ are much larger than the relative amplitudes of the normal state conductance fluctuations $\delta G_n/G_n$. However, it should be noted that the measured $I_c R_n$ product is not a constant in our device, but shows a variation between $4 \mu\text{V}$ and $34 \mu\text{V}$. These values overall are significantly lower than the value of $I_c R_n \sim \Delta/e = 150 \mu\text{V}$ expected for an ideal S-N-S junction embedding a short and diffusive normal conductor. Such reduced experimental $I_c R_n$ values compared to theory were also found in InAs nanowire based S-N-S junctions²⁶ and can typically be attributed to premature switching due to thermal activation in a capacitively and resistively shunted junction and to finite transparency of the superconductor contacts to the InSb nanowire.⁴³

2b shows the influences of magnetic field B and temperature T on the critical current I_c of the InSb nanowire based S-N-S junction device. Here, the critical current I_c measured at back-gate voltage $V_{bg} = -935$ mV (corresponding to cut B in 1a) is plotted as a function of magnetic field B (black dots) and as a function of temperature T (red crosses). With increasing magnetic field, the critical current I_c remains constant up to $B \sim 10$ mT, followed by a smooth decrease with a critical magnetic field of $B_c \sim 30$ mT. With increasing temperature, the critical current I_c decreases instantly towards smaller values. However, at temperatures above $T \sim 0.45$ K, the critical current I_c can no longer be identified. Overall the critical current I_c is related to the change in the superconducting energy gap Δ with increasing B or T as described in Ref. 43.

We now turn to investigate the characteristics of the InSb nanowire based S-N-S junction device in the voltage bias configuration. 3a displays the differential conductance dI_{sd}/dV_{sd} of the junction

device as a function of source-drain voltage V_{sd} at the base temperature of $T = 25$ mK and the zero magnetic field. The red solid curve in the figure represents the measurements at back gate voltage $V_{bg} = -600$ mV (corresponding to cut A in 1a) at which the device shows a small I_c , while the black solid curve in the figure shows the measurements at back gate voltage $V_{bg} = -935$ mV (corresponding to cut B in 1a) at which the device exhibits a large I_c . It is seen that both curves display a series of peaks, symmetric around $V_{sd} = 0$ V. These peaks can be attributed to MAR processes. It has been shown that MAR processes in an S-N-S junction give rise to a series of structures in the differential conductance dI_{sd}/dV_{sd} at source-drain voltages $V_{sd} = 2\Delta/en$, where $n = 1, 2, 3, \dots$ corresponds to the number of carrier transfers across the junction.^{46–49} In 3a, the first three peaks are clearly visible at the voltages of $V_{sd} \sim 2\Delta/en$ with $n = 1$ to 3. From a comparison with the theory for coherent MARs in short S-N-S junctions,^{50–52} we can deduce a value of $\Delta = 150$ μ V. Note that Δ determined in this way is slightly different at different back gate voltages. Also, in both curves, a sharp peak at $V_{sd} = 0$ V is observed, due to the superconductivity induced by proximity effect in the InSb nanowire section. However, comparing the two curves in 3a, we observe that the central peak is much more pronounced at $V_{bg} = -935$ mV (black solid curve), at which the critical current I_c is large. We also observe that the overall trend of dI_{sd}/dV_{sd} with decreasing $|V_{sd}|$ differs distinctly in the two curves. At $V_{bg} = -935$ mV (black solid curve) dI_{sd}/dV_{sd} increases as $|V_{sd}|$ decreases to zero, whereas at $V_{bg} = -600$ mV (red solid curve) dI_{sd}/dV_{sd} decreases. This behavior is consistent with the our early discussion that transport through a broadened energy level in the InSb nanowire junction plays an important role in this back gate voltage range. The suppression of higher order ($n \geq 4$) MAR features in the differential conductance can be attributed to inelastic processes and loss of the carrier coherence in the multiple carrier transfers across the junction.

We now proceed to investigate the magnetic field and temperature dependences of the MAR features in the differential conductance of the S-N-S junction device. 3b displays the differential conductance dI_{sd}/dV_{sd} , on a gray scale, as a function of source-drain bias voltage V_{sd} and magnetic field B at the gate voltage $V_{bg} = -600$ mV (corresponding to cut A in 1a). Here, we observe the peaks of high differential conductance as bright lines. As the magnetic field is increased from

zero, the peaks are smoothly shifted toward lower $|V_{sd}|$, as the superconducting energy gap of the Al based electrodes is decreased. The black dashed line indicates the theoretically predicted magnetic field dependence of the superconducting energy gap $2\Delta(B)/e$, where $\Delta(B) = \Delta\sqrt{1 - (B/B_c)^2}$ and B_c is the critical magnetic field of the superconductor. We note that here the measured peak positions of the differential conductance deviate slightly from the theoretical values of $\Delta(B)$ at large B . 3c shows the differential conductance dI_{sd}/dV_{sd} as a function of source-drain bias voltage V_{sd} and temperature T at zero magnetic field and again the back gate voltage of $V_{bg} = -600$ V. As the temperature is increased, the MAR peaks in the differential conductance again move toward lower $|V_{sd}|$, corresponding to a decrease of the superconducting energy gap of the Al based electrodes. The black dashed line represents the theoretically predicted temperature dependent superconducting energy gap $2\Delta(T)/e$, where $\Delta(T) = \Delta\sqrt{\cos[(\pi/2)(T/T_c)^2]}$ and T_c is the critical temperature of the superconductor. From the temperature-dependent measurements, we deduce a zero-temperature superconducting energy gap $\Delta \sim 148 \mu\text{V}$ and critical temperature $T_c \sim 0.92$ K for the Al based electrodes.

4a displays the source-drain current I_{sd} (red solid curve) measured as a function of source-drain voltage V_{sd} at back gate voltage $V_{bg} = -935$ mV, zero magnetic field, and temperature $T = 25$ mK. The measurements show clearly that the $I_{sd} - V_{sd}$ curve at the source-drain voltages of $V_{sd} > 2\Delta_0/e$ does not extrapolate back to $I_{sd} = 0$ at $V_{sd} = 0$, but to a finite excess current I_{exc} (see the black solid line in the figure). The excess current, formally the difference between I_{sd} and the normal state current at $V_{sd} \gg \Delta/e$, arises due to an interplay of currents carried by particles undergoing zero and one Andreev reflections when traversing the junction at large bias voltages.⁵⁰⁻⁵² The excess current is of particular interest, since it contains information on the junction properties and is, in contrast to I_c , practically insensitive to decoherence for transparent S-N-S junctions. 4b shows the behavior of I_{exc} as a function of temperature T (red crosses) and as a function of magnetic field B (black dots). With increasing T , the excess current I_{exc} first decreases slowly up to $T \sim 0.4$ K and then decreases quickly until it reaches zero at a temperature of $T \sim 0.95$ K. With increasing B , the excess current I_{exc} decreases smoothly towards zero. Theory^{46,52} predicts that $I_{exc} \propto \Delta$ at a

given V_{bg} and, therefore, the observed decrease of I_{exc} with increasing B or T is well explained by the corresponding decrease in Δ . However, we note that at $B \sim 30$ mT, a kink in I_{exc} is observed with a following tail of finite I_{exc} values up to $B \sim 39$ mT. A weak kink is actually also visible in the measured critical current I_c as a function of B shown in 2b. The origin of this kink is not clear. Finally, in 4c, we compare the behaviors of the excess current I_{exc} (black dashed curve) and the normal state conductance G_n (red solid curve) with change in back gate voltage V_{bg} . As in the case for the $I_c R_n$ product, the $I_{exc} R_n$ product is also not a constant. Here, we find a variation of I_{exc} from 0.4 nA to 34 nA, yielding an $I_{exc} R_n$ product between 60 μ V and 220 μ V with a peak value at the back gate voltage close to $V_{bg} = -1$ V. Our measured $I_{exc} R_n$ product values are clearly much smaller than the value of $8\Delta/3e \sim 400$ μ V predicted based on a short ballistic weak link model,⁴⁶ but are more comparable to the value of $(\pi^2/4 - 1)\Delta/e \sim 220$ μ V predicted based on a short diffusive weak link model.⁵³

In summary, we have reported a study of an InSb nanowire based S-N-S junction device and observed a proximity induced supercurrent and multiple Andreev reflections in the device. The critical current I_c tunable by a voltage applied to the back gate with a maximum value of $I_c = 5$ nA is observed. However, the $I_c R_n$ product is not a constant, but varies between 4 μ V and 34 μ V, substantially lower than the expected value of the device, $I_c R_n \sim \Delta/e = 150$ μ V, in the coherent, diffusive transport regime. We have also observed clear MAR structures, up to third order ($n = 3$), in the measured differential conductance of the junction device and deduced a superconducting energy gap of $\Delta \sim 150$ μ eV from the measurements. We have found that the behavior of dI_{sd}/dV_{sd} in the low source-drain bias voltage region depends on the normal state resistance R_n . At a small R_n the differential conductance dI_{sd}/dV_{sd} is overall increased as $|V_{sd}|$ is decreased toward zero, whereas at a large R_n it is decreased. We have measured the V_{sd} positions of the MAR structures as a function of the magnetic field and as a function of the temperature, and have found that both are in a good agreement with the theoretical predictions. Finally, we have examined the excess current I_{exc} and found that I_{exc} is in the range between 0.4 nA and 34 nA, yielding an $I_{exc} R_n$ product in the range between 60 μ V to 220 μ V, in the back gate voltage range of $V_{bg} = -4$ V to 2 V. The

observed superconductivity in the InSb nanowire based S-N-S junction, together with previously demonstrated large spin-orbit interaction strength and large Lande g-factor in the InSb nanowire quantum structures,²² opens up new opportunities in the design and realization of novel quantum devices and in the studies of new physics such as Majorana fermions in solid state systems.

This work was supported by the Swedish Research Council (VR), the Swedish Foundation for Strategic Research (SSF) through the Nanometer Structure Consortium at Lund University (nmC@LU), the National Basic Research Program of the Ministry of Science and Technology of China (Nos. 2012CB932703 and 2012CB932700).

References

- (1) Xia, Y.; Yang, P.; Sun, Y.; Wu, Y.; Mayers, B.; Gates, B.; Yin, Y.; Kim, F.; Yan, H. One-dimensional nanostructures: synthesis, characterization, and applications. *Adv. Mater.* **2003**, *15*, 353-387.
- (2) Huang, Y.; Duan, X.; Cui, Y.; Lauhon, L. J.; Kim, K.-H.; Lieber, C. M. Logic gates and computation from assembled nanowire building blocks. *Science* **2001**, *294*, 1313-1317.
- (3) Duan, X.; Huang, Y.; Wang, J.; Lieber, C. M. Indium phosphide nanowires as building blocks for nanoscale electronic and optoelectronic devices. *Nature* **2001**, *409*, 66-69.
- (4) Gudiksen, M. S.; Lauhon, L. J.; Wang, J.; Smith, D. C.; Lieber, C. M. Growth of nanowire superlattice structures for nanoscale photonics and electronics. *Nature* **2002**, *415*, 617-620.
- (5) Johnson, J. C.; Choi, H.-J.; Knutsen, K. P.; Schaller, R. D.; Yang, P.; Saykally, R. J. Single gallium nitride nanowire lasers. *Nat. Mater.* **2002**, *1*, 106-110.
- (6) Duan, X.; Huang, Y.; Agarwal, R.; Lieber, C. M. Single-nanowire electrically driven lasers. *Nature* **2003**, *421*, 241-245.
- (7) Hua, B.; Motohisa, J.; Kobayashi, Y.; Hara, S.; Fukui, T. Single GaAs/GaAsP coaxial core-shell nanowire lasers. *Nano Lett.* **2009**, *9*, 112-116.

- (8) Tian, B.; Zheng, X.; Kempa, T. J.; Fang, Y.; Yu, N.; Huang, J.; Lieber, C. M. Coaxial silicon nanowires as solar cells and nanoelectronic power sources. *Nature* **2007**, *449*, 885-889.
- (9) Kelzenberg, M.; Turner-Evans, D. B.; Kayes, B. M.; Filler, M. A.; Putnam, M. C.; Lewis, N. S.; Atwater H. A. Photovoltaic measurements in single-nanowire silicon solar cells. *Nano Lett.* **2008**, *8*, 710-714.
- (10) Dong, Y.; Tian, B.; Kempa, T. J.; Lieber, C. M. Coaxial group III-nitride nanowire photovoltaics. *Nano Lett.* **2009**, *9*, 2183-2187.
- (11) Cao, L.; White, J. S.; Park, J.-S.; Schuller, J. A.; Clemens, B. M.; Brongersma, M. L. Engineering light absorption in semiconductor nanowire devices. *Nat. Mater.* **2009**, *8*, 643-647.
- (12) Boxberg, F.; S ndergaard, N.; Xu, H. Q. Photovoltaics with piezoelectric core-shell nanowires. *Nano Lett.* **201**, *10*, 1108-1112.
- (13) Xiang, J.; Lu, W.; Hu.; Y.; Wu, Y.; Yan, H.; Lieber, C. M. Ge/Si nanowire heterostructures as high-performance field-effect transistors. *Nature* **2006**, *441*, 489-493.
- (14) Yan, H.; Choe, H. S.; Nam, S. W.; Hu, Y.; Das, S.; Flemie, J. F.; Ellenbogen, J. C.; Lieber, C. M. Programmable nanowire circuits for nanoprocessors. *Nature* **2011**, *470*, 240-244.
- (15) Nguyen, P.; Ng, H. T.; Yamada, T.; Smith, M. K.; Li, J.; Han, J.; Meyyappan, M. Direct integration of metal oxide nanowire in vertical field-effect transistor. *Nano Lett.* **2004**, *4*, 651-657.
- (16) Ng, H. T.; Han, J.; Yamada, T.; Nguyen, P.; Chen, Y. P.; Meyyappan, M. Single crystal nanowire vertical surround-gate field-effect transistor. *Nano Lett.* **2004**, *4*, 1247-1252.
- (17) Goldberger, J.; Hochbaum, A. I.; Fan, R.; Yang, P. Silicon vertically integrated nanowire field-effect transistor. *Nano Lett.* **2006**, *6*, 973-977.
- (18) Schmidt, V.; Riel, H.; Senz, S.; Karg, S.; Riess, W.; G , U. Realization of a silicon nanowire vertical surround-gate field-effect transistor. *Small* **2006**, *2*, 85-88.

- (19) Bryllert, T.; Wernersson, L.-E.; Fröberg, L. E.; Samuelson, L. vertical high-mobility wrap-gated InAs nanowire transistor. *IEEE Electron Device Lett.* **2006**, *27*, 323-325.
- (20) Nilsson, H. A.; Deng, M. T.; Caroff, P.; Thelander, C.; Samuelson, L.; Wernersson, L.-E.; Xu, H. Q. InSb nanowire field-effect transistors and quantum-dot devices. *IEEE J. Select. Top. Quant. Electr.* **2011**, *17*, 907-914.
- (21) Roddaro, S.; Fuhrer, A.; Brusheim, P.; Fasth, C.; Xu, H. Q.; Samuelson, L.; Xiang, J.; Lieber C. M. Spin states of holes in Ge/Si nanowire quantum dots. *Phys. Rev. Lett.* **2008**, *101*, 186802.
- (22) Nilsson, H. A.; Caroff, P.; Thelander, C.; Larsson, M.; Wagner, J. B.; Wernersson, L.-E.; Samuelson, L.; Xu, H. Q. Giant, level-dependent g factors in InSb nanowire quantum dots *Nano Lett.* **2009**, *9*, 3151-3156.
- (23) Nilsson, H. A.; Karlström, O.; Larsson, M.; Caroff, P.; Pedersen, J. N.; Samuelson, L.; Wacker, A.; Wernersson, L.-E.; Xu, H. Q. Correlation-induced conductance suppression at level degeneracy in a quantum dot *Phys. Rev. Lett.* **201**, *104*, 186804.
- (24) Nadj-Perge, S.; Frolov, S. M.; Bakkers, E. P. A. M.; Kouwenhoven, L. P. Spin-orbit qubit in a semiconductor nanowire. *Nature* **2010**, *468*, 1084-1087.
- (25) Kristinsdóttir, L. H.; Cremon, J. C.; Nilsson, H. A.; Xu, H. Q.; Samuelson, L.; Linke, H.; Wacker, A. & Reimann, S. Signature of Wigner localization in epitaxially grown nanowires. *Phys. Rev. B* **2011**, *83*, 041101.
- (26) Doh, Y.-J.; van Dam, J. A.; Roest, A. L.; Bakkers, E. P. A. M.; Kouwenhoven, L. P.; De Franceschi, S. *Science* **2005**, *309*, 272-275.
- (27) van Dam, J. A.; Nazarov, Y. V.; Bakkers, E. P. A. M.; De Franceschi, S.; Kouwenhoven, L. P. Supercurrent reversal in quantum dots. *Nature* **2006**, *442*, 6677-670.

- (28) Xiang, J.; Vidan, A.; Tinkham, M.; Westervelt, R. M.; Lieber, C. M. Ge/Si nanowire mesoscopic Josephson junctions *Nature Nanotech.* **2006**, *1*, 208-213.
- (29) Jespersen, T. S.; Polianski, M. L.; Sørensen, C. B.; Flensberg, K. & Nygård, J. Mesoscopic conductance fluctuations in InAs nanowire-based SNS junctions. *New J. Phys.* **2009**, *11*, 113025.
- (30) Hofstetter, L.; Csonka, S.; Nygård, J.; Schönenberger C. Cooper pair splitter realized in a two-quantum-dot Y-junction. *Nature* **2009**, *461*, 960-963.
- (31) De Franceschi, S.; Kouwenhoven, L. P.; Schönenberger C.; Wernsdorfer, W. Hybrid superconductor-quantum dot devices. *Nature Nanotech.* **2010**, *5*, 703-711.
- (32) Caroff, P.; Wagner, J. B.; Dick, K. A.; Nilsson, H. A.; Jeppsson, M.; Deppert, K.; Samuelson, L.; Wallenberg, L. R.; Wernersson, L.-E. High-quality InAs/InSb nanowire heterostructures grown by metal-organic vapor-phase epitaxy. *Small* **2008**, *4*, 878-882.
- (33) Lugani, L.; Ercolani, D.; Rossi, F.; Salviati, G.; Beltram, F.; Sorba, L. Faceting of InAs-InSb heterostructured nanowires. *Crystal growth & Design* **2010**, *10*, 4038-4042.
- (34) Vurgaftman, I.; Meyer, J. R.; Ram-Mohan, L. R. Band parameters for III-V semiconductor and their alloys *J. Appl. Phys.* **2001**, *89*, 5815-5875.
- (35) Isaacson, R. A. Electron spin resonance in n-type InSb. *Phys. Rev.* **1968**, *169*, 312-314.
- (36) Kitaev, A. Y. Unpaired Majorana fermions in quantum wires. *Phys.-Usp.* **2001**, *44*, 131-136.
- (37) Lutchyn, R. M.; Sau, J. D.; Das Sarma, S. Majorana fermions and a topological phase transition in semiconductor-superconductor heterostructures. *Phys. Rev. Lett.* **2010**, *105*, 077001.
- (38) Oreg, Y.; Refael, G.; von Oppen, F. Helical liquid and Majorana bound state in quantum wires. *Phys. Rev. Lett.* **2010**, *105*, 177002.

- (39) Akhmerov, A. R.; Dahlhaus, J. P.; Hassler, F.; Wimmer, M.; Beenakker, C. W. J. Quantized Conductance at the Majorana Phase Transition in a Disordered Superconducting Wire. *Phys. Rev. Lett.* **2011**, *106*, 057001.
- (40) Flensberg, K. Non-Abelian Operations on Majorana Fermions via Single-Charge Control. *Phys. Rev. Lett.* **2011**, *106*, 090503.
- (41) Lutchyn, R. M.; Stanescu, T. D.; Das Sarma, S. Search for Majorana fermions in multiband semiconductor nanowires. *Phys. Rev. Lett.* **2011**, *106*, 127001.
- (42) Stanescu, T.; Lutchyn, R. M.; Das Sarma S. Majorana fermions in semiconductor nanowires. arXiv:1106.3078 (2011).
- (43) Tinkham, M. *Introduction to Superconductivity* (Dover, New York, 1996).
- (44) Tinkham, M.; Free, J. U.; Lau, C. N.; Markovic, N. Hysteretic I-V curves of superconducting nanowires. *Phys. Rev. B* **2003**, *68*, 134515.
- (45) Beenakker, C. W. J.; van Houten, H. Josephson current through a superconducting quantum point contact shorter than the coherence length. *Phys. Rev. Lett.* **1991**, *66*, 3056-3059.
- (46) Klapwijk, T. M.; Blonder, G. E.; Tinkham, M. Explanation of subharmonic energy gap structure in superconducting contacts. *Physica B+C* **1982**, *109-110*, 1657-1664.
- (47) Octavio, M.; Tinkham, M.; Blonder, G. E.; Klapwijk, T. M. Subharmonic energy-gap structure in superconducting constrictions. *Phys. Rev. B* **1983**, *27*, 6739-6746.
- (48) Flensberg, K.; Hansen, B.; Octavio, M. Subharmonic energy-gap structure in superconducting weak links. *Phys. Rev. B* **1988**, *38*, 8707-8711.
- (49) Kleinsasser, A. W.; Miller, R. E.; Mallison, W. H.; Arnold, G. B. Observation of multiple Andreev reflections in superconducting tunneling junctions. *Phys. Rev. Lett.* **1994**, *72*, 1738-1741.

- (50) Bratus, E. N.; Shumeiko, V. S.; Wendin, G. Theory of subharmonic gap structure in superconducting mesoscopic tunnel contacts. *Phys. Rev. Lett.* **1995**, *74*, 2110-2113.
- (51) Averin, D.; Bardas, A. ac Josephson effects in a single quantum channel. *Phys. Rev. Lett.* **1995**, *75*, 1831-1834.
- (52) Cuevas, J. C.; Martin-Rodero, A.; Yeyati, A. L. Hamiltonian approach to the transport properties of superconducting quantum point contacts. *Phys. Rev. B* **1996**, *54*, 7366-7379.
- (53) Artemenko, S. N.; Volkov, A. F.; Zaitsev, A. V. Theory of nonstationary Josephson effect in short superconducting contacts. *Sov. Phys. JETP* **1979**, *49*, 924-931.

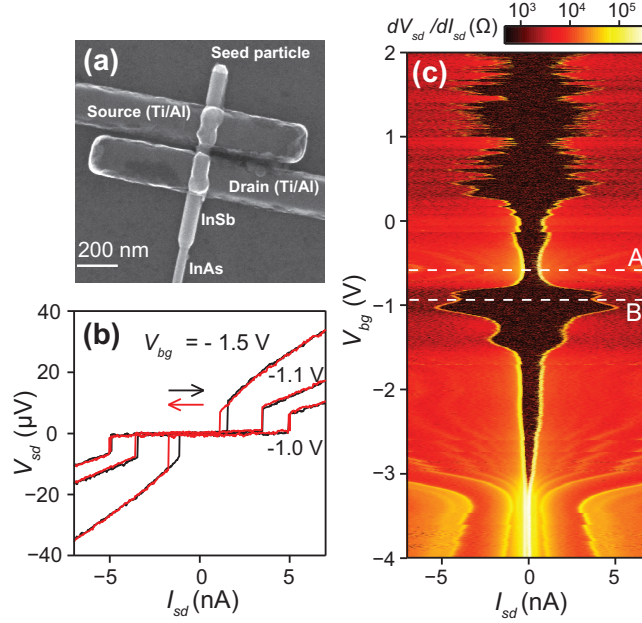


Figure 1: (a) SEM image of an InSb nanowire based S-N-S junction device. The device is made from the InSb segment of an InAs/InSb heterostructure nanowire with Ti/Al metal contacts, on a SiO_2 capped, highly doped Si substrate, using electron beam lithography. (b) Source-drain voltage V_{sd} measured for the device as a function of the source-drain current I_{sd} at three different gate voltages $V_g = -1.5$, -1.1 , and -1.0 V, and at base temperature $T = 25$ mK. The black curves are recorded in the upward current sweeping direction and the red curves in the downward current sweeping direction. The hysteresis is seen in the V_{sd} - I_{sd} characteristics of the device measured at $V_{bg} = -1.5$ V. A supercurrent is seen to flow through the InSb nanowire segment, due to superconductivity induced by the proximity effect, in the regions with negligible source-drain voltages. A critical current I_c can be identified as an applied current at which the measured source-drain voltage jumps to a finite value. (c) Differential resistance dV_{sd}/dI_{sd} , on a color scale, as a function of the source-drain current I_{sd} and the silicon back gate voltage V_{bg} , measured at base temperature $T = 25$ mK. The central dark area corresponds to a region with negligible device resistance (superconductivity region). The critical current I_c , which can be identified from the edge of the dark area, varies strongly with V_{bg} .

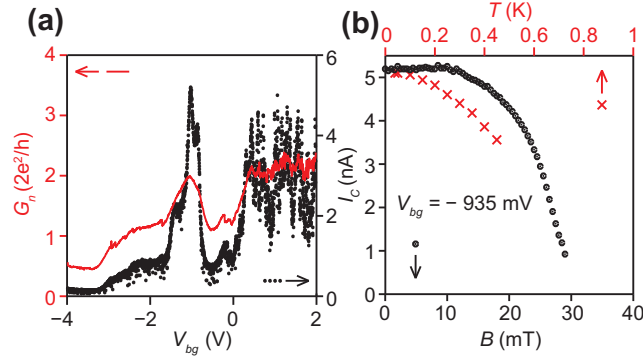


Figure 2: (a) Normal state conductance G_n (red solid curve) and critical current I_c (black dots) measured against back gate voltage V_{bg} at base temperature $T = 25$ mK. The normal state conductance in the linear response regime is measured at magnetic field $B = 100$ mT larger than the critical field B_c of the superconductor Al. The measurements show that the $I_c R_n$ product is not a constant in the device, but varies between $4 \mu\text{V}$ and $34 \mu\text{V}$. (b) Critical current I_c measured as a function of magnetic field B (black dots) and as a function of temperature T (red crosses) at back gate voltage $V_{bg} = -935$ mV (corresponding to cut B in 1a). With increasing magnetic field B , I_c remains constant up to $B \sim 10$ mT and then decreases smoothly with a critical magnetic field of $B_c \sim 30$ mT. With increasing temperature T , I_c decreases instantly. But at temperatures above $T = 0.45$ K, I_c can no longer be identified from the measurements.

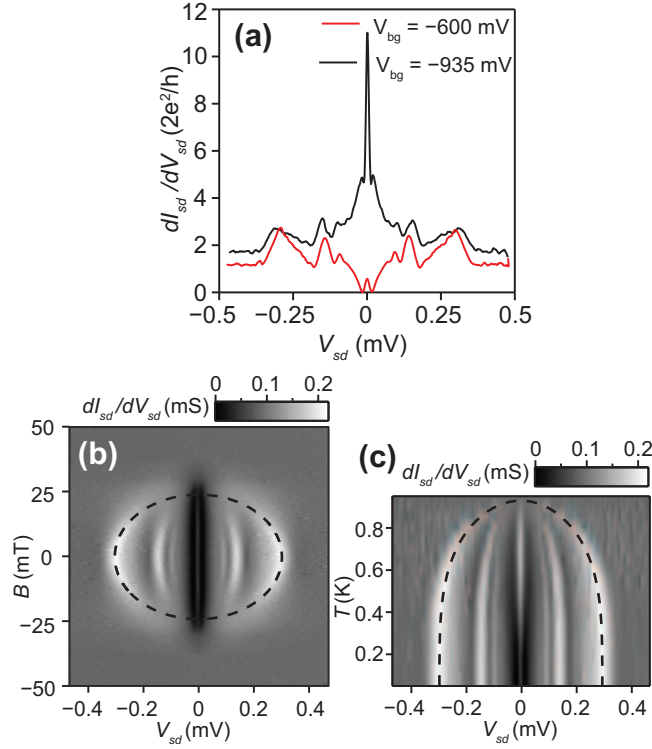


Figure 3: (a) Differential conductance dI_{sd}/dV_{sd} measured as a function of source-drain voltage V_{sd} at back gate voltage $V_{bg} = -935$ mV (black solid curve, corresponding to cut B in 1c) and $V_{bg} = -600$ mV (red solid curve, corresponding to cut A in 1c) at base temperature $T = 25$ mK. Both curves are seen to display a series of peaks, due to MARs, symmetric around $V_{sd} = 0$ V. The two curves also show different behaviors in the magnitude of dI_{sd}/dV_{sd} as $|V_{sd}|$ is decreased to zero. The black solid curve shows that dI_{sd}/dV_{sd} increases on average, followed by a strong supercurrent peak at $V_{sd} = 0$ V, while the red solid curve shows that dI_{sd}/dV_{sd} decreases on average, followed by a strongly suppressed supercurrent peak at $V_{sd} = 0$ V. (b) Differential conductance dI_{sd}/dV_{sd} , on a gray scale, measured as a function of source-drain bias voltage V_{sd} and magnetic field B at base temperature $T = 25$ mK and gate voltage $V_{bg} = -600$ mV. Here, the peaks in dI_{sd}/dV_{sd} are seen as bright white lines. The black dashed line indicates the theoretically predicted magnetic field dependence of the superconducting energy gap of the Al based electrodes. (c) Differential conductance dI_{sd}/dV_{sd} , on a gray scale, measured as a function of source-drain bias voltage V_{sd} and base temperature T at zero magnetic field and back gate voltage $V_g = -600$ mV. The black dashed curve displays the theoretically predicted temperature dependence of the superconducting energy gap of the Al based electrodes.

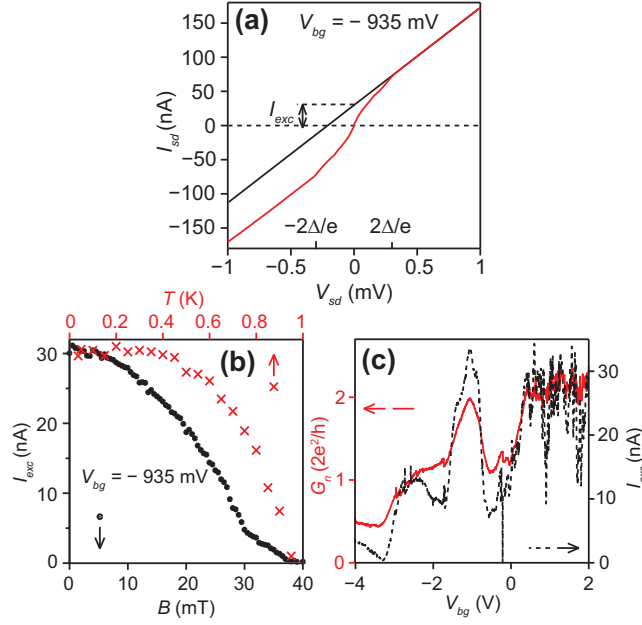


Figure 4: (a) Source-drain current I_{sd} (red solid curve) as a function of source-drain bias V_{sd} measured at base temperature $T = 25$ mK and back gate voltage $V_{bg} = -935$ mV (corresponding to cut B in 1a). The current I_{sd} at large $V_{sd} > 2\Delta/e$ is linear in V_{sd} . However, it does not extrapolate back to zero at $V_{sd} = 0$ V, but to a finite excess current I_{exc} . (b) Excess current I_{exc} as a function of temperature T (red crosses) and as a function of magnetic field B (black dots) extracted for the device at back gate voltage $V_{bg} = -935$ mV (corresponding to cut B in 1a). (c) Normal state conductance G_n (red solid curve) and excess current I_{exc} (black dots) plotted against back gate voltage V_{bg} for the device at base temperature $T = 25$ mK. The normal state conductance is measured in the linear response regime at magnetic field $B = 100$ mT $> B_c$ (the same as in 2a). The $I_{exc}R_n$ product extracted from the measurements varies between $60 \mu\text{V}$ and $220 \mu\text{V}$.